WALL INTERACTION EFFECTS FOR A FULL-SCALE HELICOPTER ROTOR IN THE NASA AMES 80- BY 120-FOOT WIND TUNNEL

Patrick M. Shinoda
US Army Aviation RD&E Center - ATCOM
and
NASA Ames Research Center
Moffett Field, California 94035-1000

SUMMARY

A full-scale helicopter rotor test was conducted in the NASA Ames 80- by 120-Foot Wind Tunnel with a four-bladed S-76 rotor system. This wind tunnel test generated a unique and extensive data base covering a wide range of rotor shaft angles-of-attack and rotor thrust conditions from 0 to 100 knots. Three configurations were tested: empty tunnel; test stand body (fuselage) and support system; and, fuselage and support system with rotor installed. Empty tunnel wall pressure data are evaluated as a function of tunnel speed to understand the baseline characteristics. Aerodynamic interaction effects between the fuselage and the walls of the tunnel are investigated by comparing wall, ceiling, and floor pressures for various tunnel velocities and fuselage angles-of-attack. Aerodynamic interaction effects between the rotor and the walls of the tunnel are also investigated by comparing wall, ceiling, and floor pressures for various rotor shaft angles, rotor thrust conditions, and tunnel velocities. Empty tunnel wall pressure data show good repeatability and are not affected by tunnel speed. In addition, the tunnel wall pressure profiles are not affected by the presence of the fuselage apart from a pressure shift. Results do indicate that the tunnel wall pressure profiles are affected by the presence of the rotor. Significant changes in the wall, ceiling, and floor pressure profiles occur with changing tunnel speeds for constant rotor thrust and shaft angle conditions. Significant changes were also observed when varying rotor thrust or rotor shaft angle-of-attack. Other results indicate that dynamic rotor loads and blade motion are influenced by the presence of the tunnel walls at very low tunnel velocity and, together with the wall pressure data, provide a good indication of flow breakdown.

LIST OF SYMBOLS

A	rotor disk area, πR^2, ft^2
b	number of rotor blades
c	airfoil chord length, ft
C_P	test section wall pressure coefficient, $(P_W - P_{SCLT}) / Q_{PSF}$
C_S	speed of sound, ft/s
C_T	rotor thrust coefficient, perpendicular to tip-path-plane, $T/A\rho(\Omega R)^2$
C_T/σ	rotor thrust coefficient divided by rotor solidity, $T/\rho(\Omega R)^2 S_R$
M_{TIP}	rotor tip Mach number, $\Omega R/C_S$
P_{SCLT}	calculated test section centerline static pressure referenced to outside ambient pressure based on P_R and P_S, lb/ft^2
P_R	test section total pressure referenced to outside ambient pressure, lb/ft^2
P_S	test section static pressure referenced to outside ambient pressure, lb/ft^2
P_W	test section wall pressure (west wall, east wall, tunnel ceiling, tunnel floor) referenced to outside ambient pressure, lb/ft^2
Q_{PSF}	test section free-stream dynamic pressure, lb/ft^2
R	rotor radius, ft
S_R	rotor blade area, bcR, ft^2
T	rotor thrust, positive up, lb
V_∞	free-stream velocity, ft/s
x	distance upstream of rotor centerline, ft
α_F	fuselage angle, positive nose up, deg
α_s	rotor shaft angle ($\alpha_F = \alpha_s$), positive aft of vertical, deg
μ	advance ratio, $V_\infty/\Omega R$
ρ	free-stream air density, slug/ft^3
σ	rotor solidity, $bc/\pi R$ or S_R/A
σ	standard deviation
Ω	rotor rotational speed, rad/s

1.0 INTRODUCTION

Wind tunnel testing has been extensively used in the development and improvement of rotorcraft designs, in addition to providing a data base for refinement of theoretical predictions. However, in the low-speed flight regime (0 to 60 kt) of rotorcraft wind tunnel testing (small-scale and specifically full-scale), there is no significant rotor performance, rotor loads, or rotor control state data base with which prediction codes can be validated. Some of the major reasons for this lack of information are: 1) the inability to properly account for wind tunnel wall corrections when the rotor produces large downwash angles at low speed/high thrust conditions; 2) the difficulty in identifying the onset of flow breakdown (the point at which standard wall corrections can no longer correct to free air) for a given rotor and wind tunnel test section size; 3) the difficulty in accounting for Reynolds number effects for small-scale rotors; and, 4) the inability of the tunnel to operate at low speeds for certain size rotors.

There have been wind tunnel tests to establish certain facilities' capabilities / limitations for testing rotorcraft in the low-speed flight regime. Studies have been conducted at the University of Washington (Refs. 1 - 3) and Boeing Vertol Company (Refs. 4, 5) to understand the flow breakdown phenomenon in a wind tunnel with a rotor present. These studies provided some guidelines in determining when flow breakdown will occur for a given size rotor and wind tunnel cross-section, and insights into identifying when flow breakdown occurs. All of these investigations used small-scale rotors.

A full-scale Sikorsky S-76 rotor test was recently conducted in the NASA Ames 80- by 120-Foot Wind Tunnel. In Ref. 6 the facility was evaluated for hover testing and rotor forward flight performance data were correlated with analytical results and other test data. The wide-field shadowgraph technique was evaluated for visualizing full-scale rotor wakes from this test in Ref. 7. One of the main objectives of this test was to establish a data base of information documenting the tunnel's capability to operate a full-scale rotor system throughout its low-speed flight

Presented at an AGARD Meeting on 'Wall Interference, Support Interference and Flow Field Measurements', October 1993.

envelope, including into the tunnel flow breakdown region. This data base will assist in establishing wall corrections for future rotor tests in this facility (using Glauert (Ref. 8), Heyson (Refs. 9-12), Joppa (Refs. 13-14), or Hackett and Wilsden (Ref. 15), Hackett, Wilsden, and Lilley (Ref. 16) methodologies or a combination of them), establish the flow breakdown region for this general size rotor system and wind tunnel, and assist in refinement of theoretical predictions for rotor systems in the low-speed flight regime.

The focus of this paper is to investigate the interaction between the S-76 rotor and the wind tunnel walls. The approach in this investigation was to: (1) acquire empty tunnel wall pressure data and evaluate the baseline characteristics as a function of tunnel speed; (2) acquire data for the fuselage alone and support system configuration to investigate aerodynamic interaction effects between the fuselage and the walls of the tunnel for different tunnel speeds and fuselage angles-of-attack; (3) acquire data for the fuselage with the rotor installed configuration to evaluate rotor inflow and wake effects (by varying tunnel speed, shaft angle, and thrust condition) on wind tunnel test section wall and floor pressures; and, (4) establish the criteria for flow breakdown for this rotor and wind tunnel cross-sectional area.

This paper presents a brief description of the experiment. Wall pressure measurements are discussed and evaluated with the tunnel empty, with the fuselage present, and with the fuselage and rotor present. Various rotor conditions are explored including the flow breakdown regime. Finally, concluding remarks of the research results are presented.

2.0 DESCRIPTION OF THE EXPERIMENT

NASA Ames 80- by 120-Foot Wind Tunnel

The 80- by 120-Foot Wind Tunnel is part of the National Full-Scale Aerodynamics Complex (NFAC) located at the NASA Ames Research Center. The tunnel has an open circuit with a closed, rectangular test section. The maximum test section flow speed is approximately 100 knots. Figure 1 shows a schematic of the wind tunnel circuit. The 80- by 120-Foot Wind Tunnel shares a portion of the flow circuit with the 40- by 80-Foot Wind Tunnel; both tunnels share a single drive system. The drive system consists of six fans rated at 135,000 maximum combined horsepower (101 MW). When operating in the 80 x 120 mode, a system of vanes and louvers are positioned so that the 40 x 80 circuit is closed off and the 80 x 120 leg forms a through-flow wind tunnel (Fig. 1). The drive fans pull outside air in through the 80 x 120 inlet and exhaust the air back to the atmosphere through louvers in the tunnel wall downstream of the tunnel fan drive system.

The test section is 80 ft high, 120 ft wide, and 193 ft long. The east wall of the test section has two doors that provide an access opening of approximately 80 ft in height by 120 ft in width. This opening provides room for the tunnel crane to move into the test section for installation of various size wind tunnel models.

General Hardware

The experiment used a production Sikorsky Aircraft S-76 rotor system. The rotor was mounted on NASA's modified Rotor Test Apparatus (RTA). Figure 2 shows the model installed in the wind tunnel. The rotor system is four-bladed with coincident flap and lag articulation provided at the blade root by elastomeric bearings. Blade pitch is also permitted by the same bearing through the rotor spindle. Table 1 lists the S-76 main rotor parameters. The rotor system, including the hub, spindles, blades, and swashplate is identical to the production model.

The RTA is a special-purpose test stand used for operating helicopter rotors in the NFAC. The test stand was originally built in the mid-1970's. The RTA houses two electric-drive motors, a right-angle transmission, a new rotor balance with 22,000 lb thrust capability (installed in 1992) along with primary and dynamic control systems. The primary control system consists of three electro-hydraulic servo-actuators with an on-board hydraulic system with accumulators. The dynamic control system is integrated into the primary control system and provides time varying perturbation capability to the non-rotating swashplate. The RTA was first built as a body of revolution that was 33.3 ft in length and had a maximum diameter of 5.83 ft. In 1991, the RTA was modified to incorporate a fairing on top to enclose the raised rotor control system and the new balance. The new fairing on top of the RTA is 15.96 ft in length and has a maximum cross-section (3.5 ft wide by 4 ft tall) located near the rotor shaft .

The RTA was mounted in the wind tunnel on a three-strut (two main struts and one tail strut) support system placing the rotor hub nominally one rotor diameter above the wind tunnel floor. The model angle-of-attack was varied by changing the height of the gimballed tail strut. All data presented in this paper were acquired with the first harmonic flapping trimmed to near zero.

Instrumentation

The new RTA rotor balance provides increased accuracy in measuring rotor hub loads. This five-component rotor balance measures rotor lift, drag and side forces, together with the rotor pitching and rolling moments. Also incorporated is an instrumented flex coupling to measure rotor torque. Both rotor balance and flex coupling are designed to measure static and dynamic loads. Table 2 lists the general capabilities of the rotor balance.

To understand the interaction effects between the rotor and the wind tunnel at various test conditions, the walls, ceiling, and floors were instrumented with static pressure taps: 21 taps on both east and west walls at mid-height, 21 taps on the centerline of the ceiling, and 18 taps on the floor forward of the rotor shaft and 2 ft to starboard from the centerline of the rotor and tunnel. Refer to Figs. 3-4 for streamwise pressure tap locations. Table 3 lists the general capabilities of the pressure transducers used in this experiment.

Test Configurations and Conditions

Three basic test configurations were investigated: empty tunnel (speed sweep), fuselage and support system (speed sweep at specific fuselage angles-of-attack), and fuselage and support system with the rotor installed (speed sweeps at specific thrusts and rotor shaft angles-of-attack, and thrust sweeps at specific speeds and shaft angles-of attack). The full range of test conditions for each configuration is shown in Tables 4-7. Since the 80 x 120 is an open circuit wind tunnel, outside winds can affect the tunnel test section conditions. To alleviate this concern, the majority of low speed testing was performed when the ambient outside wind speeds were less than 5 kt and the air speed through the test section was less than 4 kt (based on tunnel dynamic pressure measurements).

Wall Pressure Data Reduction and Uncertainty Analysis

The primary parameter used to quantify the effects of the fuselage and rotor on the tunnel walls is the pressure coefficient, Cp.

The wall pressure coefficients were obtained using the following equation,

$$C_P = \frac{(P_W - P_{SCLT})}{Q_{PSF}} \tag{1}$$

Given that $P_{SCLT} = (P_R - P_S)(-1.1936)$, the equation is expanded to

$$C_P = \frac{(P_W - (P_R - P_S)(-1.1936))}{Q_{PSF}} \qquad (2)$$

An uncertainty analysis, based on Refs. 17-18, was performed to determine the error estimate for the wall pressure coefficients. The analysis requires the partial derivative of Cp with respect to each measurement parameter in Eq. 2; in addition, the estimate of the standard deviation is needed for each parameter. The error estimate for Cp is represented by,

$$\sigma_{C_P} = \left[\left(\frac{\partial C_P}{\partial P_W}\right)^2 \sigma_{P_W}^2 + \left(\frac{\partial C_P}{\partial P_R}\right)^2 \sigma_{P_R}^2 + \left(\frac{\partial C_P}{\partial P_S}\right)^2 \sigma_{P_S}^2 + \left(\frac{\partial C_P}{\partial Q_{PSF}}\right)^2 \sigma_{Q_{PSF}}^2 \right]^{\frac{1}{2}} \qquad (3)$$

where

σ_{P_W} = standard deviation of the wall pressure
= calibration accuracy / 2

σ_{P_R} = standard deviation of the test section total pressure
= calibration accuracy / 2

σ_{P_S} = standard deviation of the test section static pressure
= calibration accuracy / 2

$\sigma_{Q_{PSF}}$ = standard deviation of the free-stream dynamic pressure
= calibration accuracy / 2

Uncertainty analysis results for wall pressure coefficients at various tunnel speeds are shown in Table 8. As expected, the uncertainty level increases with decreasing tunnel speeds; this was caused primarily by the uncertainty in Q_{PSF} at low speeds.

3.0 EMPTY TUNNEL RESULTS

The purpose of acquiring the empty tunnel wall pressure data was to establish the baseline wall pressure distribution of the tunnel as a function of tunnel speed. Repeat empty tunnel runs were performed to document the repeatability of the measurements for various tunnel speeds.

Effects Of Tunnel Velocity On Cp Values

The effects of tunnel velocity on the west wall Cp values are presented in Fig. 5. The data show tunnel velocity has no effect on the west wall pressure distribution profile except for minimal offsetting in the pressure distribution. The measurements on the east wall, ceiling and floor are similar and within uncertainty levels for the various tunnel speeds.

Repeatability of Empty Tunnel Run Data

Figure 6 demonstrates the repeatability of pressure coefficient data along the west wall at tunnel velocities of 100 kt and 20 kt. At 100 kt, the total variation in the wall pressure coefficient from pressure tap to pressure tap is quite small (less than 0.04) and the individual pressure tap variation is even smaller (less than 0.01). The 20 kt case shows a slight increase in random fluctuations (up to 0.03) between the individual transducers for a given distribution. However, the overall pressure distribution is similar to the 100 kt profile except for a mean offset. This can probably be attributed to error in the measurement system. The east wall, ceiling, and floor pressures all show similar results as the west wall pressures.

4.0 FUSELAGE ALONE EFFECTS ON WALL PRESSURES

One of the objectives of this test was to investigate the aerodynamic interaction between the fuselage (including the support strut system) and the walls of the tunnel. This was done by comparing the empty tunnel wall pressure data with data acquired with the fuselage installed at various angles-of-attack.

Effect of Fuselage on Tunnel Wall Pressures

Figures 7 and 8 present the effect of the fuselage and support struts on the tunnel west wall and floor pressure distributions, respectively, for a tunnel speed of 100 kt and a fuselage angle-of-attack of -2 deg. Results for the east wall and ceiling are similar to the west wall.

The shape of the pressure profile for the west wall with the fuselage installed, shown in Fig. 7, does not vary significantly from the empty tunnel data. However, the pressure distribution does shift in a negative direction. According to Hackett et al (Ref. 16), a local reduction in area caused by the presence of a body in the tunnel free-stream should create a local reduction in wall pressure in the vicinity of the fuselage / support struts, but not an entire profile shift as shown in the figure. The shift may be attributed to a blockage effect from the body and support struts causing more than just a local effect on the tunnel wall pressures. However, the blockage for α_F= -2 deg is estimated to be approximately 2 percent.

The floor pressure profile, shown in Fig. 8, shows there is a significant effect when the fuselage and support struts are present. When the fuselage is present, the pressure coefficient at the furthest upstream location matches closely to the empty tunnel floor pressure coefficients. As the rotor centerline is approached, the pressure coefficient becomes more positive and reaches its maximum value near the rotor centerline. Aft of the rotor shaft centerline, the pressure becomes less positive and more closely matches the empty tunnel floor pressures in this location. This can be attributed to the proximity of the pressure taps on the floor to the right main strut fairing. The main strut fairings are 3.5 ft thick by approximately 8.5 ft in chord length at the floor. The 3-strut support system creates a blockage effect causing the air to flow between the wall and the support system. This causes a low-velocity, high-pressure region forward of the struts where the floor pressures are measured.

The effect of tunnel speed on the tunnel wall pressures with the fuselage present was also analyzed. The pressure profiles for 60 kt were similar to the 100 kt profiles. For velocities less than or equal to 40 kt, the measurements showed consistent negative shifts. These indicated shifts in wall pressure distributions below 40 kt can be partially attributed to limitations of the measurement capabilities of the transducers. Another cause of this shift may be a blockage effect from the body and support struts causing more than just a local effect on the tunnel wall pressures.

Effect of Fuselage Angle on Tunnel Wall Pressures

The effect of fuselage angle-of-attack on a west wall pressure tap is shown for 100 kt in Fig. 9. The data are taken from a representative pressure tap located at the longitudinal station nearest to the test section turntable centerline (turntable centerline is zero in Fig. 3). A similar location was chosen to evaluate the east wall and ceiling pressure data; for the floor, the pressure tap furthest upstream was chosen.

In Fig. 9, the differences in C_P between the fuselage installed and the empty tunnel is at a maximum when $\alpha_F=10$ deg then decreases as the fuselage angle decreases and becomes nearly zero at $\alpha_F= -15$ deg. This trend indicates that the blockage effect of the fuselage and support system can be minimized by selecting an appropriate fuselage angle-of-attack. The strut-blockage effect appears to be counteracted by the fuselage as the angle-of-attack is decreased to -15 deg. The east wall, ceiling, and floor pressure coefficient values show similar results as the west wall data. For speeds less than 100 kt, the effects of the fuselage on the west wall and the other wall pressures were similar to the 100 kt condition. The lower speed conditions, however, exhibited an increase in uncertainty (as shown in Table 8).

5.0 ROTOR/FUSELAGE EFFECT ON WALL PRESSURES

The following section discusses the effect of the combined rotor / fuselage configuration on the wind tunnel wall pressures. The wall pressures are evaluated for different rotor advance ratios, thrust levels, and shaft angles. These three parameters influence the strength and location of the rotor wake.

Effect of Advance Ratio

Figures 10 - 13 present the effect of the rotor wake on the tunnel walls, ceiling, and floor as the advance ratio is varied. The rotor thrust coefficient-to-solidity ratio is 0.10 and the rotor shaft angle is tilted forward 2 deg during this advance ratio sweep.

The west wall pressure coefficients are shown in Fig. 10. The wall pressure profiles for $\mu \geq 0.06$ (24 kt) are similar to the empty tunnel profiles except for a mean offset. However, for $\mu<0.06$ (24 kt), a low pressure region begins to appear; the region increases in size and magnitude and moves forward towards the rotor centerline as advance ratio is decreased. Norman and Yamauchi (Ref. 19) observed similar results for a full-scale helicopter rotor (46 ft diameter) in the NASA Ames 40- by 80-Foot Wind Tunnel.

The east wall pressure profile, Fig. 11, is similar to the west wall profile except for a few differences and in general, agrees with observations of Rae (Ref. 1) and Norman and Yamauchi (Ref. 19). The east wall low pressure region appears at an advance ratio of $\mu=0.06$ (24 kt) and the peak low pressure region is slightly forward in position and greater in magnitude than the west wall pressure (compare Fig. 10 and Fig. 11). These differences are caused by the variation in wake strength and shape due to the direction of rotor rotation; the east wall is on the advancing blade side of the rotor and the west wall is on the retreating blade side of the rotor.

The strength, size and location of the low pressure regions and peaks shown in Figs. 10 and 11 are directly related to the rotor wake skew angle (a function of rotor inflow ratio and advance ratio) and rotor height in the tunnel. As advance ratio decreases the rotor wake skew angle decreases, which moves the rotor wake impingement on the floor further upstream underneath and closer to the rotor. This means the rotor wake rollup along both walls moves upstream, therefore, causing the peak low pressure region on both walls to move upstream closer to the rotor. As observed by Rae (Ref. 1), this condition can cause flow recirculation in the tunnel and the onset of reverse flow on the tunnel side walls as the peak low pressure region moves closer to the rotor centerline (see $\mu=0.03$ (12 kt) case in Fig. 11).

Figure 12 shows the tunnel ceiling pressure distribution is affected by the rotor system throughout the advance ratio range studied but to a lesser degree than the east and west walls. Above $\mu=0.113$ (45 kt), the pressure signature is relatively small in magnitude upstream of the rotor and still compares well with the empty tunnel pressure profile. The pressure signature becomes more pronounced as the advance ratio is decreased below 0.113 (45 kt). However, contrary to expectations, the low pressure regional peak does not move downstream as advance ratio is decreased. For hover condition, the peak should be directly above the rotor. Recirculation effects may be influencing the rotor inflow.

In Fig. 13, advance ratio does not have an affect on the floor pressure profile above $\mu=0.113$ (45 kt). However, as the advance ratio is decreased to 0.06 (24 kt), a positive shift in the pressure level occurs with no significant change in profile. This positive shift can be partially attributed to the measurement system uncertainties. However, the majority of the shift may be attributed to the increasing influence of the rotor wake as the tunnel speed is decreased. In particular, the rotor wake may cause a partial blockage (this blockage is a function of skew angle) resulting in a reduction in the local free-stream velocity below and in front of the rotor relative to the surrounding region. For $\mu=0.04$ (16 kt) , a very small profile distortion occurs upstream of the rotor centerline possibly representing the beginning of a small ground vortex. At $\mu=0.03$ (12 kt), a large profile distortion is generated further upstream of the rotor. At this point, the downwash of the rotor begins to strongly interact with free-stream air below the rotor creating a ground vortex and a large low pressure region. Also, the large positive pressures beneath the rotor are caused by the impingement of the wake on the floor. Evidence of ground vortices have also been observed by Rae (Ref. 2) and Sheridan and Wiesner (Ref. 4). These results are further discussed in the section on flow breakdown. These studies showed that the vortex becomes stronger and moves upstream as tunnel speed is decreased.

Effect of Rotor Thrust

The effect of rotor thrust on the tunnel walls (east and west) and ceiling pressure distributions are shown in Figs. 14, 15, and 16, respectively. The advance ratio is fixed at 0.05 (20 kt) and the rotor shaft angle is tilted forward 2 deg during this thrust sweep.

Both west and east wall show a low pressure region forming aft of the rotor at $C_T/\sigma=0.08$. This low pressure region expands in size and strength with increasing thrust. In addition, the low pressure region peak moves upstream closer to the rotor centerline as the thrust is increased. This behavior was also observed by Norman and Yamauchi (Ref. 19). Again when comparing the east and west wall pressure profiles for a given thrust condition, the east wall pressure profile distortion is larger and closer to the rotor than the west wall.

The strength, size and location of the low pressure regions and peaks shown in Figs. 14 and 15 can once again be directly related to the rotor wake skew angle and rotor height in the tunnel. As the thrust increases, the rotor wake skew angle decreases which moves the rotor wake impingement on the floor further upstream. Thus, the location where the wake flows up the walls also moves upstream and gains strength due to increased thrust. Subsequently, the peak low pressure region on both walls becomes stronger and moves upstream closer to the rotor. Note that increasing thrust has the same effect on the location of the low pressure region peak as decreasing advance ratio.

The effect of thrust on the ceiling pressure profile is shown in Fig. 16. The ceiling pressure profile is affected for all thrust levels at this advance ratio. The magnitude of the low pressure regional peaks increase with thrust as expected, however, the peaks remain stationary instead of moving downstream with increasing thrust. This expected movement in peaks may exist but was not observed possibly due to coarse spacing of pressure taps.

Effect of Rotor Shaft Angle

The effects of rotor shaft angle on the tunnel west wall, east wall, ceiling and floor pressure distribution profiles are shown in Figs. 17 - 22 for $C_T/\sigma=0.10$ at fixed advance ratios. The side walls and ceiling profiles are shown at $\mu=0.05$ (20 kt) and the floor pressures at $\mu=0.03$ (12 kt).

Figures 17 and 18 show the east and west wall pressures have similar profiles and that shaft angle has a minimal effect on the wall pressure profiles. As noted in earlier sections of this paper, the east wall low pressure region is more clearly defined, of greater magnitude, and further upstream than the west wall. The strength, size and location of the low pressure regions and peaks shown in Figs. 17 and 18 are also related to the rotor wake skew angle, rotor shaft tilt, and rotor height in the tunnel. As the shaft angle is increased from -10 deg to 5 deg, the rotor wake impingement on the floor is expected to move further upstream, together with wake roll-up, toward the rotor. This would cause the low pressure region and the peak to move upstream closer to the rotor and have a greater magnitude. However as discussed earlier, this is not occurring.

The ceiling pressure profiles, shown in Fig. 19, are similar in shape for each shaft angle. For any given shaft angle, the low pressure region peaks remain stationary instead of moving downstream with increasing shaft angle; this was also observed with rotor thrust sweeps discussed earlier.

The cause for the side wall peaks not moving upstream and ceiling peak downstream with decreasing shaft angle may be due to the coarse distribution of pressure taps, or more extreme shaft angles are required to cause movement of the low pressure region of the wall and ceiling profiles.

A review of the ceiling pressure profile data indicates a relationship between the pressure distortion peak strength and shaft angle for a given advance ratio. Figures 20 and 21 show this relationship in absolute magnitudes for advance ratios of 0.03 - 0.06 (12 - 24 kt), 0.10 (40 kt), and 0.25 (100 kt). The pressure peak magnitude on the ceiling increases with increasing rotor shaft angle for all advance ratios. Even though the uncertainty estimates are large at these low advance ratios, there is a definite trend.

Figure 22 presents the effect of the rotor shaft angle on the tunnel floor pressure distribution at $\mu=0.03$ (12 kt). This speed was chosen since no effects on tunnel floor pressure distribution occurred at $\mu=0.05$ (20 kt) (see Fig. 13). However, as shown earlier in this section, there is a significant effect at $\mu=0.03$ (12 kt). Figure 22 shows the general pressure profile does not change with rotor shaft angle but there is an indication that the low pressure region moves forward with increasing shaft angle which is expected.

6.0 FLOW BREAKDOWN

The results from the previous section showed the effect of the rotor on the wind tunnel. Ultimately, the goal is to determine what effect the wind tunnel has on the rotor and to determine (for this size rotor system) at what condition (rotor thrust, rotor shaft angle-of-attack, and tunnel speed) the wind tunnel environment becomes an inadequate substitute for the free-air environment. The other term commonly used to describe this condition is flow breakdown: where wall corrections are no longer sufficient to correct to free air conditions (Ref. 2). Establishing this flow breakdown envelope for this size rotor will assist future test programs in establishing a proper test matrix that avoids this area of rotor / tunnel operation.

Flow breakdown usually occurs at a tunnel speed where the rotor wake begins to create a ground vortex, placing the rotor in-ground effect (Refs. 2 and 4). For full-scale testing, installing a rotor out of ground effect for a hover condition in a wind tunnel is rarely possible. Sheridan and Wiesner (Ref. 4) describe how deviations in the steady-state rotor controls and rotor power appear as tunnel speed is reduced to a ground effect or flow breakdown condition. The data from this investigation do not reveal such deviations. However, floor pressure results presented in Figs. 13 and 22 do indicate the presence of a ground vortex; in addition, Figs. 10 and 11 show strong wall pressure distribution distortions at the same advance ratio of $\mu=0.03$ (12 kt). These changes in the floor and advancing blade side-wall pressure distribution were also observed in Rae's tests (Refs. 1-3). The following discusses some of the dynamic rotor loads and blade motion results that show indications of flow breakdown that correspond to the floor pressure and wall pressure results.

Dynamic (1/2 peak-to-peak) rotor loads and blade motion results are shown in Figs. 23 and 24, respectively, for three thrust conditions and a rotor shaft angle of -2 deg.

Rotor thrust 1/2 peak-to-peak loads, shown in Fig. 23, increase with decreasing tunnel speed and peak between 30 and 40 kt (depending on the fixed thrust condition) and then decrease until 12 to 16 kt is reached. This vibratory load could be expected to continually decrease to a lower value in hover. Instead, the unsteady thrust is found to increase to a higher level and almost matches the same vibratory condition at 30 to 40 kt. Similar results are seen in other dynamic rotor and blade loads data. This is probably due to an unsteady and strong rotor wake recirculation caused by the enclosed test section walls.

Figure 24 shows a similar trend for rotor blade 1/2 peak-to-peak flap motion. The blade flap motion reaches a minimum at 70 kt as advance ratio is decreased from 100 kt. As the velocity is further decreased, the flapping motion gradually increases and peaks between 30 and 40 kt, and then decreases until 12 to 16 kt is reached. As the velocity is reduced further, the flapping motion increases to a much higher level.

The data shown in Figs. 23 and 24 correlate well with the west and east wall pressure data and floor pressure data (Figs. 10, 11, and 13, respectively) presented earlier in this paper. The east and west wall pressure profiles begin to show a strong low pressure peak at $\mu= 0.04$ (16 kt) and even a stronger one at $\mu= 0.03$ (12 kt). These results are similar to Rae's experiments (Refs. 1 and 3) but at different advance ratios; the level of distortion in the pressure distribution seen in Fig. 11 at $\mu= 0.04$ (16 kt) and below is what Rae considered to be indicative of flow breakdown. The floor pressure distribution shows this large change in pressure profile at $\mu= 0.03$ (12 kt) also indicating a ground vortex formation upstream of the rotor, again similar to Rae's experiment (Ref. 2). The ground vortex in combination with the rotor wake recirculation in the test section, shown in the pressure data, grows and causes an increase in rotor unsteadiness manifested in both rotor loads and blade motion as the tunnel speed is decreased. The 12 - 16 kt region corresponds to the inflection point of the rotor 1/2 peak-to-peak thrust data and blade flapping motion data. Therefore, wall pressures as well as rotor oscillatory loads indicate flow breakdown occurs at or below $\mu= 0.04$ (16 kt) for a shaft angle of -2 deg at these particular thrust conditions for this facility.

7.0 CONCLUDING REMARKS

A full-scale helicopter rotor test was conducted in the NASA Ames 80- by 120-Foot Wind Tunnel with a four-bladed S-76 rotor system. This wind tunnel test generated a unique and extensive data base covering a wide range of rotor shaft angles-of-attack and rotor thrust conditions from 0 to 100 knots. Three configurations were tested: empty tunnel; test stand body (fuselage) and support system; and fuselage and support system with rotor installed. The study has resulted in the following observations.

Empty Tunnel

Wall pressure coefficient values and profiles are not affected by tunnel speed. The mean offsets in wall Cp profiles are well within the uncertainty estimates.

Wall pressure data show good repeatability within the uncertainty analysis calculations.

Fuselage Alone

Wall pressure data with the fuselage installed are similar when compared with empty tunnel data. However, the fuselage does have an effect by shifting the pressure distribution profile relative to the empty tunnel profile. The magnitude of this shift depends on the body angle-of-attack and tunnel speed.

Minimum blockage of the wind tunnel does not occur at 0 deg fuselage angle-of-attack but at -15 deg.

Fuselage and Rotor

The east wall, west wall and floor pressures are affected by the presence of the rotor only at low speeds. An effect of rotor thrust was also observed but to a lesser degree.

The ceiling pressures are affected by the presence of the rotor at all speed and shaft angles at high thrust conditions. The magnitude of this effect is a function of shaft angle, speed, and thrust condition.

Flow Breakdown

The dynamic rotor loads, dynamic blade flapping motion, and wall and floor pressures indicate flow breakdown occurs at or below $\mu = 0.04$ (16 kt).

ACKNOWLEDGEMENTS

The author acknowledges the significant efforts of the NASA test team in the conduct of this experimental investigation. Special thanks to Dr. Alan Wadcock for his technical assistance in this paper. The author also recognizes Lee Helmle and Cynthia Freedman of Sterling Software for their development of the pressure plotting program that allowed the review of large sets of data in a minimum amount of time.

REFERENCES

1. Rae, W. H., Jr., "Limits on Minimum-Speed V/STOL Wind-Tunnel Tests," *Journal of Aircraft*, Vol. 4, No. 3, May-June 1967, pgs. 249-254.
2. Rae, W. H., Jr., "An Experimental Investigation of Wind Tunnel Wall Corrections and Test Limits for V/STOL Wind-Tunnel Tests," U.S. Army Grant No. DA-ARO-31-124-G-809, Project No. 4506-E , AD-764 255, Dept. of Aeronautics and Astronautics, Univ. of Washington, July 1973.
3. Rae, W. H., Jr. and Shindo, S., "An Experimental Study of Alleviating the Limits on Minimum Speed V/STOL Wind Tunnel Tests," University of Washington, Dept. of Aeronautics and Astronautics, Report No.68-1, 1968.
4. Sheridan, P. F. and Wiesner, W., "Aerodynamics of Helicopter Flight Near the Ground," American Helicopter Society 33rd Annual Forum, Washington D.C., May 1977.
5. Harris, F. D., "Aerodynamic and Dynamic Rotary Wing Model Testing in Wind Tunnels and Other Facilities," Advisory Group for Aerospace Research and Development (AGARD) Lecture Series No. 63, May 1973.
6. Shinoda, P. M, and Johnson, W., "Performance Results from a Test of an S-76 Rotor in the NASA Ames 80- by 120-Foot Wind Tunnel," AIAA Paper 93-3414, AIAA Eleventh Applied Aerodynamics Conference, Monterey, CA, August 1993.
7. Swanson, A., "Application of the Shadowgraph Flow Visualization Technique to a Full-Scale Helicopter in Hover and Forward Flight," AIAA Paper 93-3411, AIAA Eleventh Applied Aerodynamics Conference, Monterey, CA, August 1993.
8. Glauert, H., " The Interference on the Characteristics of an Airfoil in a Wind Tunnel of Rectangular Section," R & M 1459, 1932.
9. Heyson, H. H., "Linearized Theory of Wind Tunnel Jet Boundary Corrections and Ground Effect for VTOL-STOL Aircraft," NASA TR R-124, 1962.
10. Heyson, H. H., "Jet-Boundary Corrections for Lifting Rotors Centered in Rectangular Wind Tunnels," NASA TR R-71, 1960.
11. Heyson, H. H., "Use of Superpositions in Digital Computers to Obtain Wind-Tunnel Interference Factors for Arbitrary Configurations, With Particular Reference to V/STOL Vehicles," NASA TR R-302, 1969.
12. Heyson, H. H., "General Theory of Wall Interference for Static Stability Tests in Closed Rectangular Test Sections and in Ground Effect," NASA TR R-364, 1971.
13. Joppa, R. G., "A Method of Calculating Wind Tunnel Interference Factors for Tunnels of Arbitrary Cross Section," NASA CR-845, 1967.
14. Joppa, R. G., " Wind Tunnel Interference Factors for High-Lift Wings in Closed Wind Tunnels," NASA CR-2191, February 1973.
15. Hackett, J. E. and Wilsden, D. J., "Determination of Low Speed Wake Blockage Corrections via Tunnel Wall Static Pressure Measurements," AGARD CP 174, Paper 23, October 1975.
16. Hackett, J. E., Wilsden, D. J., and Lilley, D. E., "Estimation of Tunnel Blockage from Wall Pressure Signatures: A Review of Data Correlation," NASA CR 152,241, March 1979.
17. Kline, S. J. and McClintock, F. A., "Describing Uncertainties in Single-Sample Experiments," *Mechanical Engineering*, January 1953.
18. Schenk, H., Theories of Engineering Experimentation, McGraw-Hill, 1979.
19. Norman, T. R. and Yamauchi, G. K., "Full-Scale Investigation of Aerodynamic Interactions Between a Rotor and Fuselage," American Helicopter Society 47th Annual Forum, Phoenix, AZ, May 1991.

Table 1. Main Rotor Parameters

Parameter	Value	
Radius	22	ft
Nominal Chord	15.5	in
Solidity Ratio	.0748	
Number of Blades	4	
Airfoils	SC1095 and SC1095R8	
Flapping Hinge offset	3.70%	radius
Lock No.	11.6	
100% RPM	293	
100% tip speed	675	fps

Table 2. RTA Rotor Balance Calibration Accuracy

			Std. Deviation of Error		
Parameter	Maximum Capacity		Value		% Capacity
Normal Force	22,000	lbs	25	lbs	0.12
Side Force	4,400	lbs	7	lbs	0.16
Axial Force	4,400	lbs	12	lbs	0.27
Pitching Moment	694,000	in-lbs	324	in-lbs	0.05
Rolling Moment	694,000	in-lbs	504	in-lbs	0.07
Torque	36,083	ft-lbs	--		--

Table 3. Pressure Transducer Accuracies

			2 Std. Deviation of Error		
Parameter	Maximum Capacity		Value		% Capacity
P_W(West Wall)	0.36	psid	0.00036	psid	0.10
P_W(East Wall)	0.36	psid	0.00036	psid	0.10
P_W(Ceiling)	0.36	psid	0.00036	psid	0.10
P_W(Floor)	1.00	psid	0.00100	psid	0.10
P_R	0.19	psid	0.00019	psid	0.10
P_S	1.00	psid	0.00080	psid	0.08
Q_{PSF}	262	psf	0.20000	psf	0.10

Table 4. Empty Tunnel Test Matrix

Tunnel Velocity, kt	4, 8, 12, 16, 20, 24, 28, 32, 36,40, 50, 60, 70, 80, 90, 100

Table 5. Fuselage Alone Test Matrix

Fuselage Angles, α_F	-15°, -10°, -5°, 0°, 5°, 10°
Tunnel Velocity, kt	0 - 100

Table 6. Speed Sweep Test Matrix

V_∞ = 0-100 kt

M_{TIP} : 0.605 (675 fps)

α_s	THRUST, lb		
	8,000 (C_T/σ=.065)	9,850 (.080)	12,320 (.100)
10°		X	X
5°	X	X	X
0°		X	
-2°	X	X	X
-5°	X	X	
-10°	X	X	X

Table 7. Thrust Sweep Test Matrix

C_T/σ=0.03-0.125

M_{TIP} : 0.605 (675 fps)

VKTS	μ	α_s					
		10°	5°	0°	-2°	-10°	-15°
20	0.050				X		
32	0.080			X			
40	0.100	X	X		X	X	X
50	0.125	X	X				
60	0.150	X	X		X	X	X
80	0.200	X	X		X	X	
100	0.250	X	X		X	X	X

Table 8. Wall Pressure Uncertainties

(+- 2σ)

VKTS	Approx Q_{PSF}	μ	West Wall C_p	East Wall C_p	Ceiling C_p	Tunnel Floor C_p
100	33.90	0.25	.004	.004	.004	.0053
80	21.67	0.20	.006	.006	.006	.0086
60	12.19	0.15	.011	.011	.011	.0153
40	5.41	0.10	.024	.024	.024	.0347
32	3.46	0.08	.037	.037	.037	.054
20	1.35	0.05	.095	.095	.095	.137
16	0.86	0.04	.157	.157	.157	.222
12	0.48	0.03	.308	.308	.308	.423

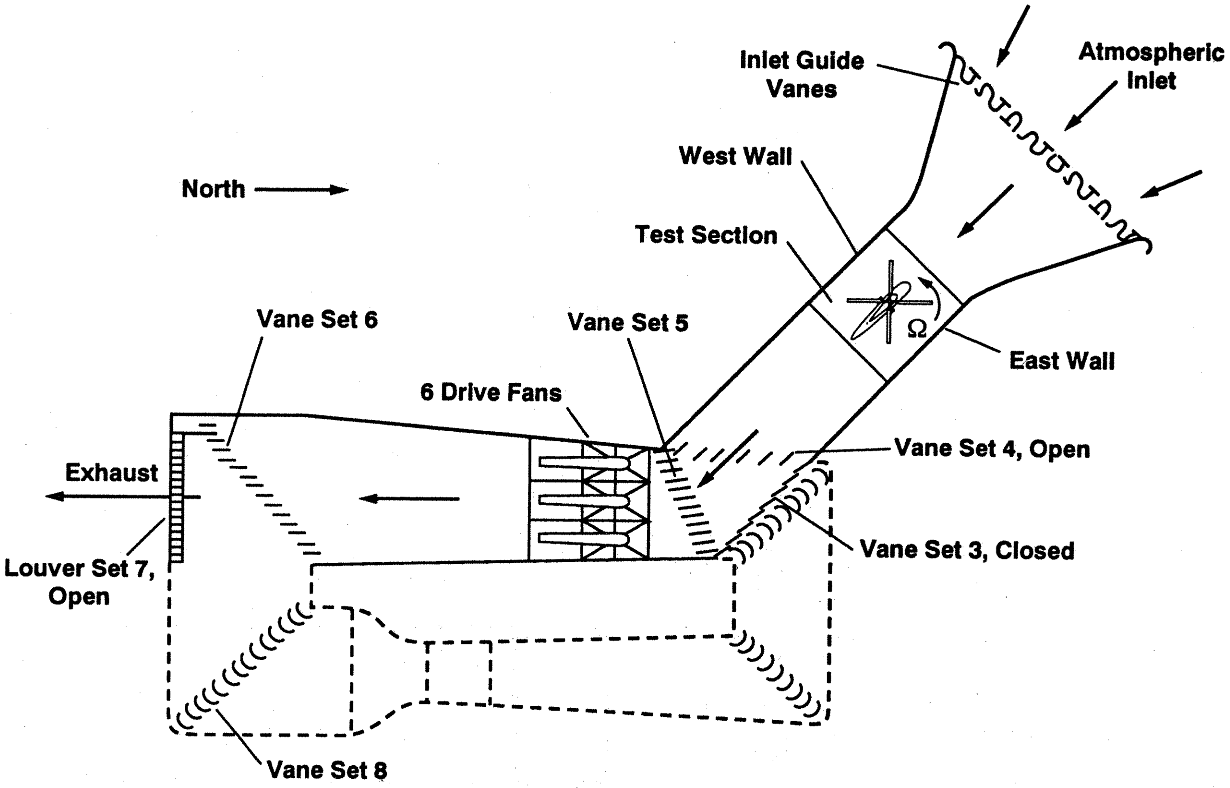

Fig. 1 80- by 120-Foot Wind Tunnel circuit.

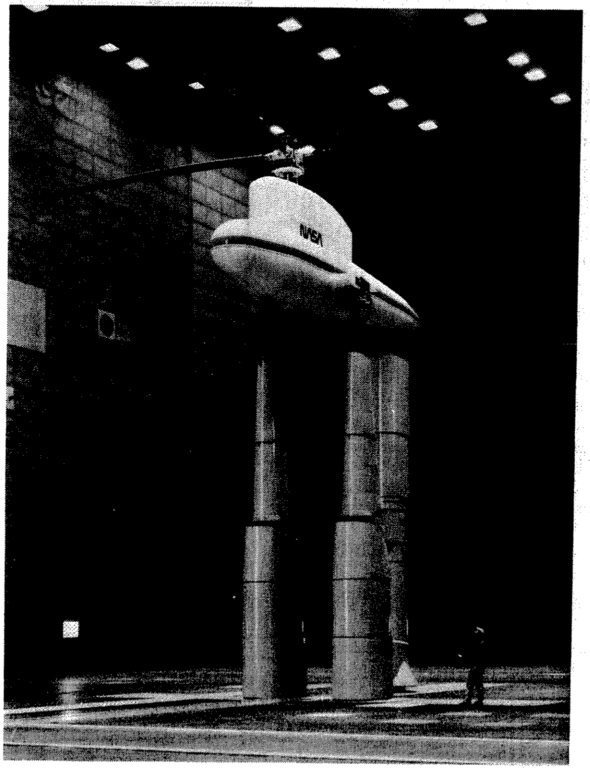

Fig. 2 S-76 Rotor System installed on Rotor Test Apparatus in the Ames 80- by 120-Foot Wind Tunnel.

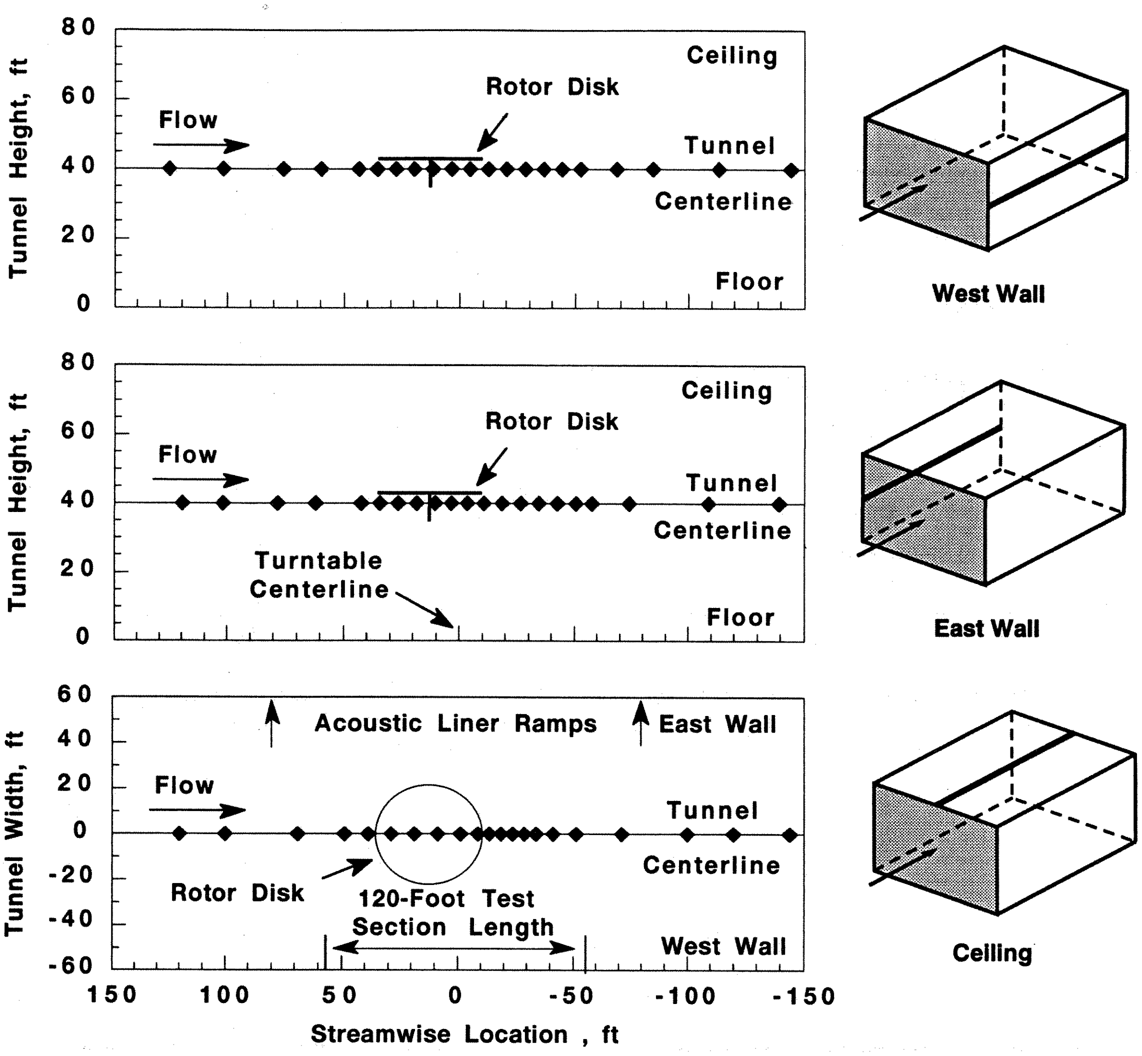

Fig. 3 West wall, east wall, and ceiling pressure tap locations in the wind tunnel.

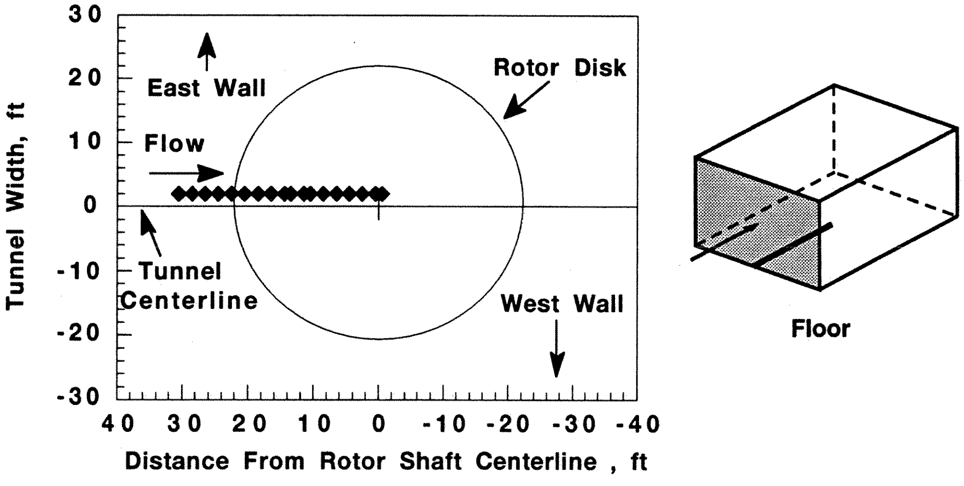

Fig. 4 Floor pressure tap locations in the wind tunnel.

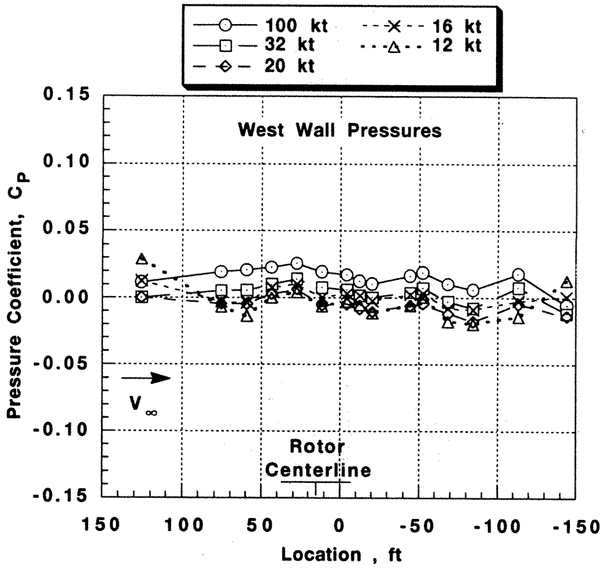

Fig. 5 Effect of tunnel speed on empty tunnel west wall pressures.

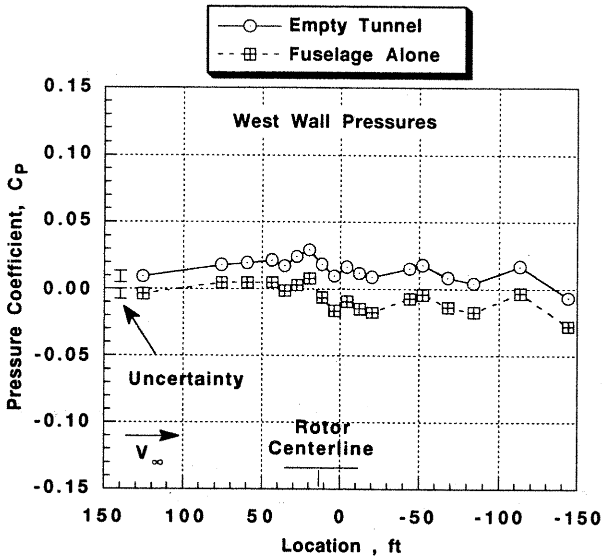

Fig. 7 Effect of fuselage on wind tunnel west wall pressures, V_∞=100 kt, α_F= –2 deg.

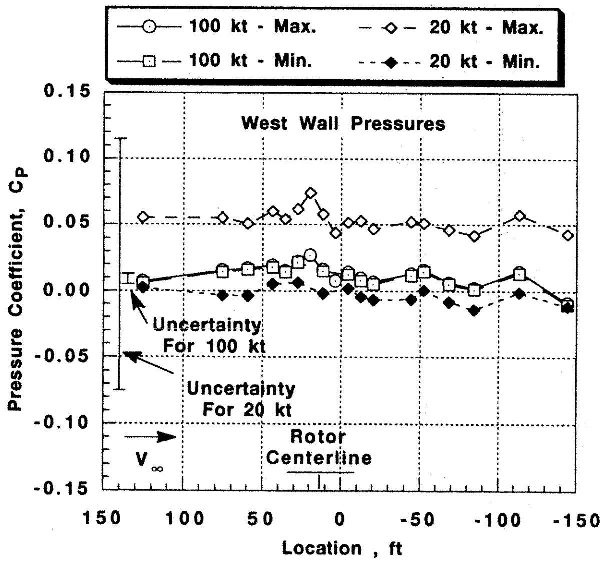

Fig. 6 Empty tunnel west wall pressure repeatability at 100 kt and 20 kt.

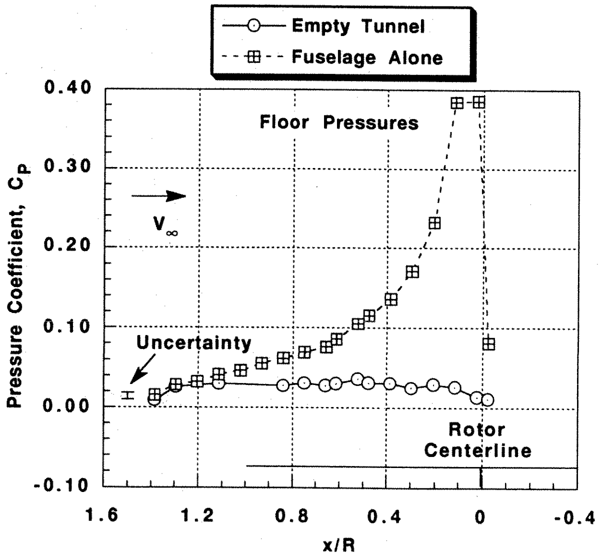

Fig. 8 Effect of fuselage on wind tunnel floor pressures, V_∞=100 kt, α_F= –2 deg.

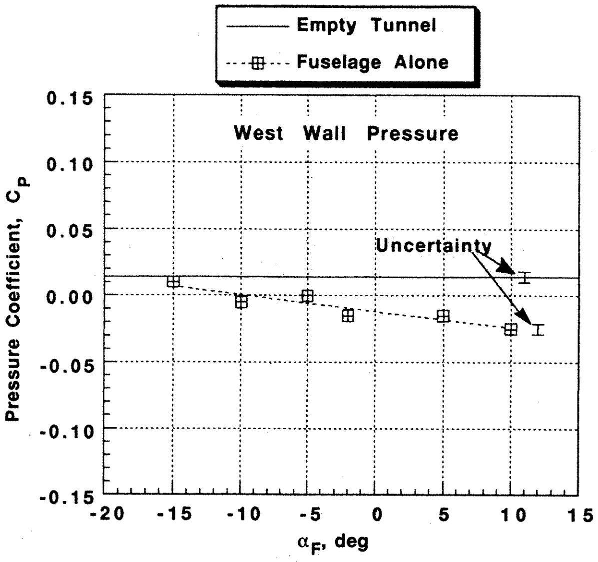

Fig. 9 Effect of angle-of-attack of fuselage on west wall pressure at 100 kt.

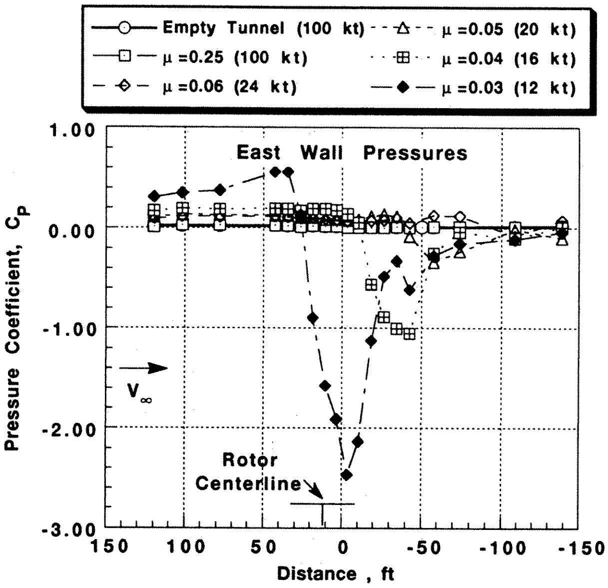

Fig. 11 Effect of advance ratio on tunnel east wall pressures; α_S= -2 deg, C_T/σ=0.100.

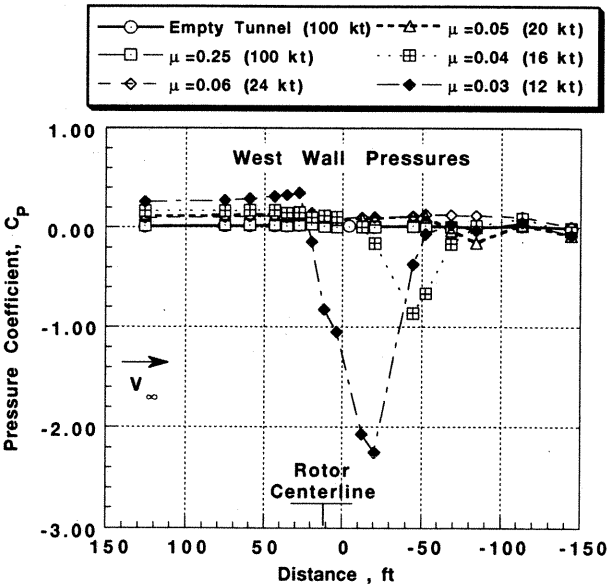

Fig. 10 Effect of advance ratio on tunnel west wall pressures; α_S= -2 deg, C_T/σ=0.100.

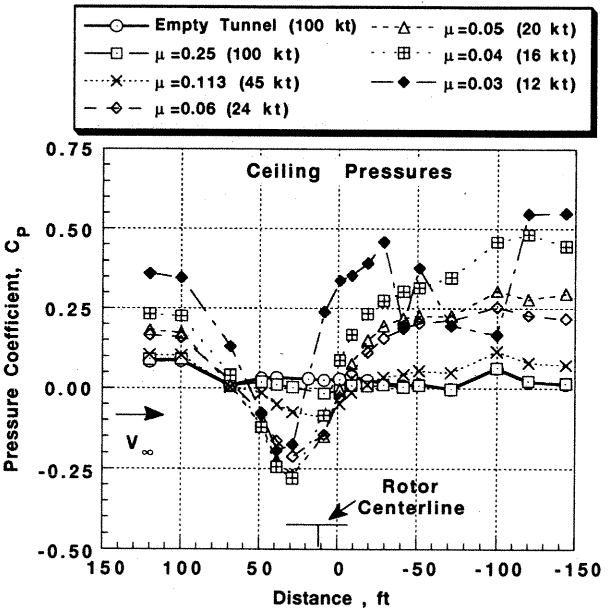

Fig. 12 Effect of advance ratio on tunnel ceiling pressures; α_S= -2 deg, C_T/σ=0.100.

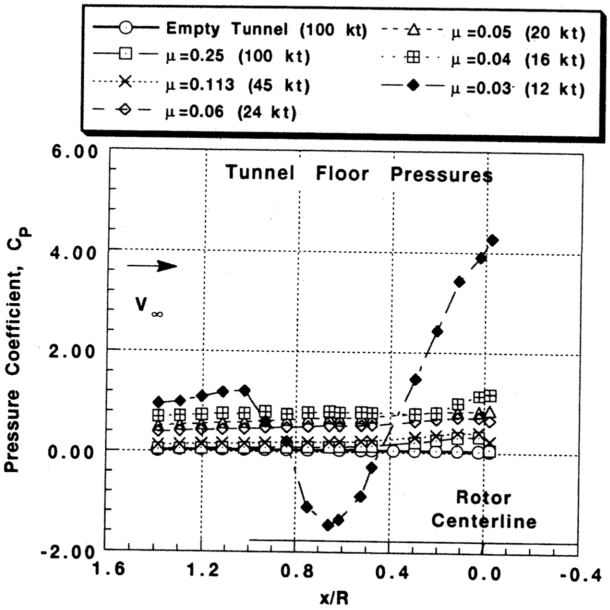

Fig. 13 Effect of advance ratio on tunnel floor pressures; α_S= -2 deg, C_T/σ=0.100.

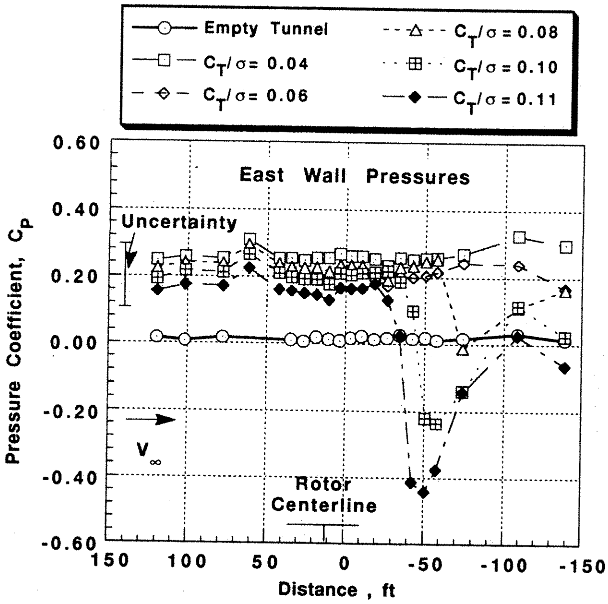

Fig. 15 Effect of rotor thrust on tunnel east wall pressures; α_S= -2 deg, μ= 0.05 (20 kt).

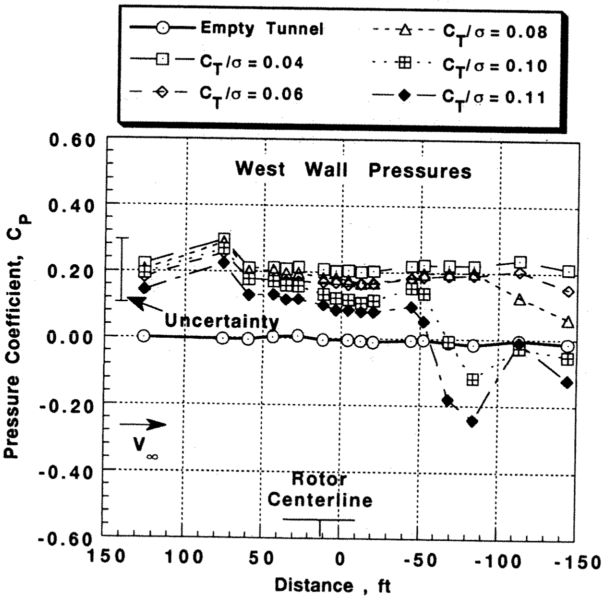

Fig. 14 Effect of rotor thrust on tunnel west wall pressures; α_S= -2 deg, μ= 0.05 (20 kt).

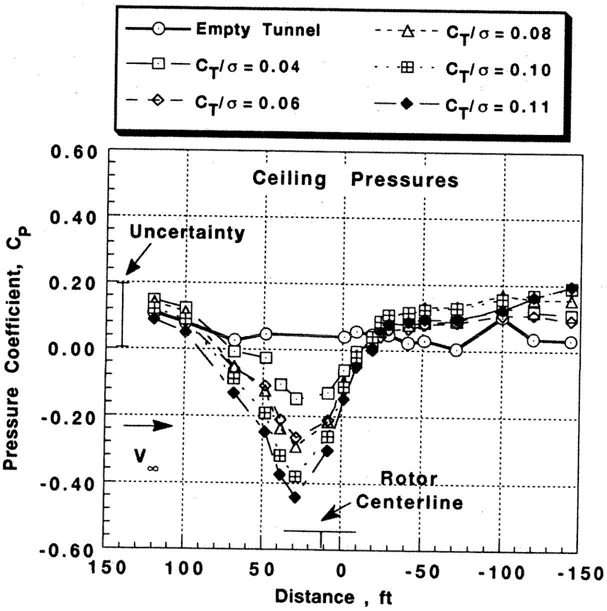

Fig. 16 Effect of rotor thrust on tunnel ceiling pressures; α_S= -2 deg, μ= 0.05 (20 kt).

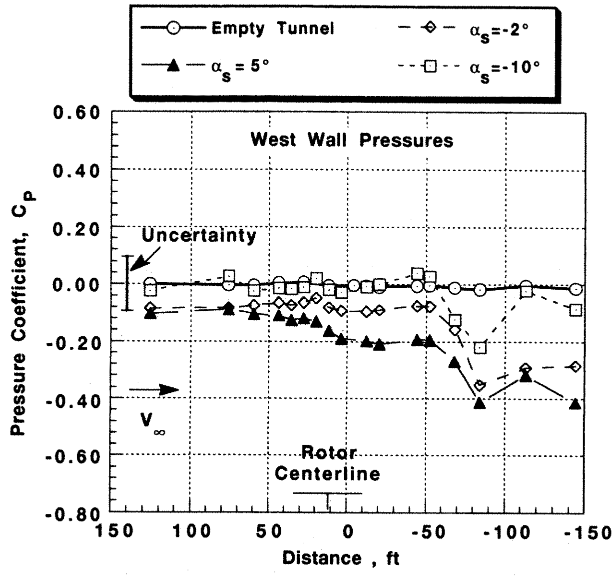

Fig. 17 Effect of rotor shaft angle-of-attack on tunnel west wall pressures; C_T/σ=0.100, μ= 0.05 (20 kt).

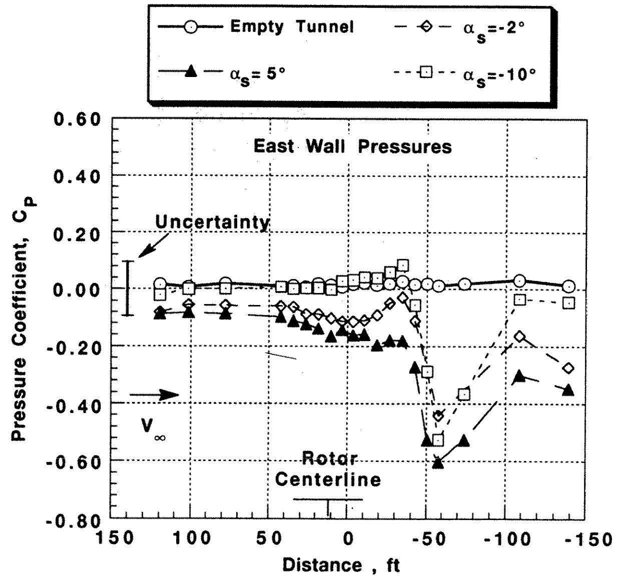

Fig. 18 Effect of rotor shaft angle-of-attack on tunnel east wall pressures; C_T/σ=0.100, μ= 0.05 (20 kt).

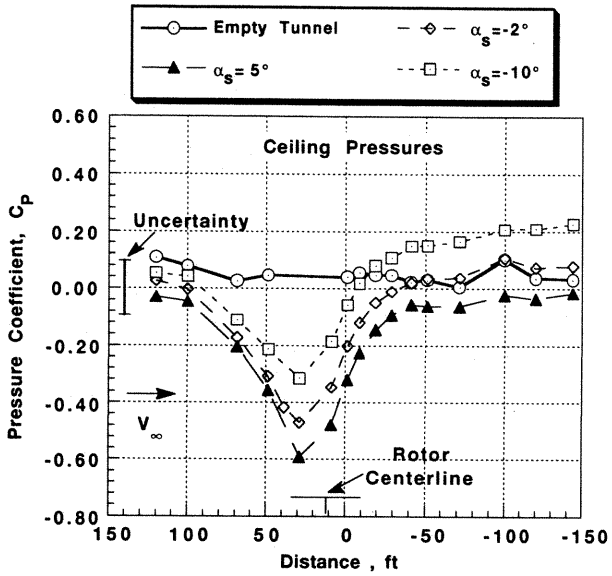

Fig. 19 Effect of rotor shaft angle-of-attack on tunnel ceiling pressures; C_T/σ=0.100, μ= 0.05 (20 kt).

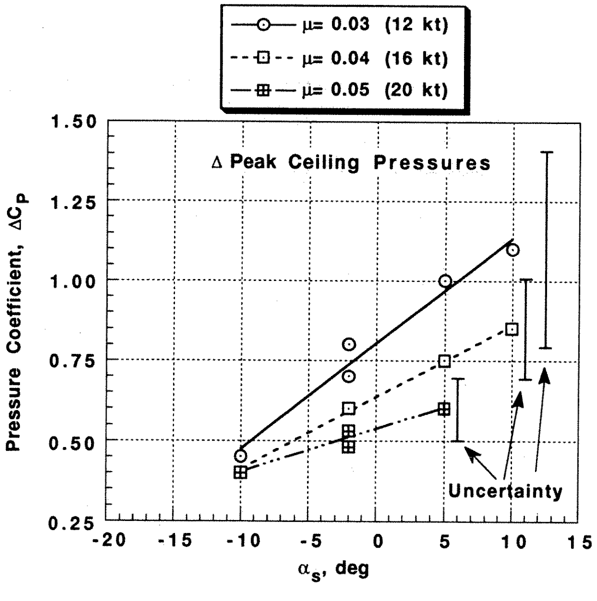

Fig. 20 Effect of rotor shaft angle-of-attack on tunnel ceiling peak wall pressures; C_T/σ=0.100, μ= 0.03 (12 kt) to 0.05 (20 kt).

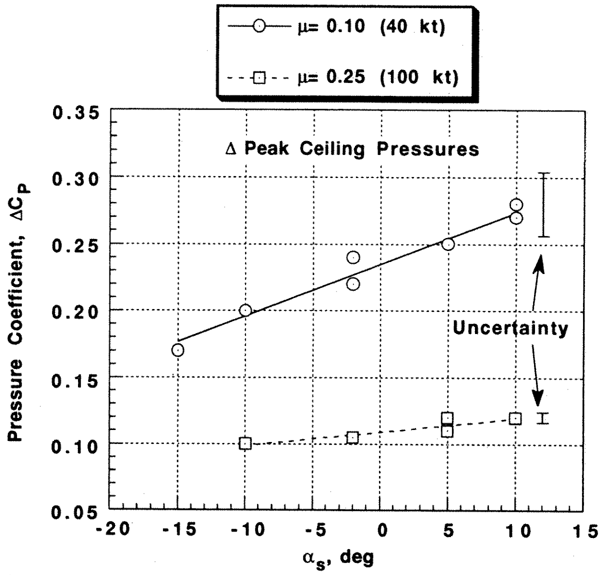

Fig. 21 Effect of rotor shaft angle-of-attack on tunnel ceiling peak wall pressures; C_T/σ=0.100, μ= 0.10 (40 kt), 0.25 (100 kt).

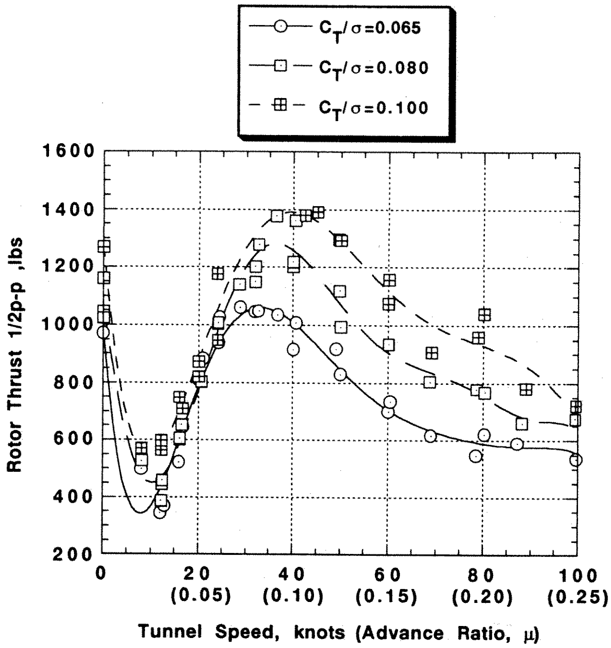

Fig. 23 Effect of advance ratio on rotor 1/2 p-p thrust; α_s= -2 deg, C_T/σ=0.065, 0.080, 0.100.

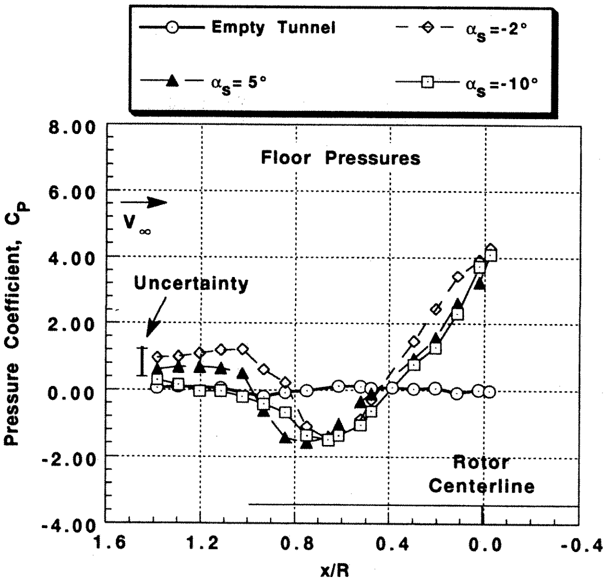

Fig. 22 Effect of rotor shaft angle-of-attack on tunnel floor pressures; C_T/σ=0.100, μ= 0.03 (12 kt).

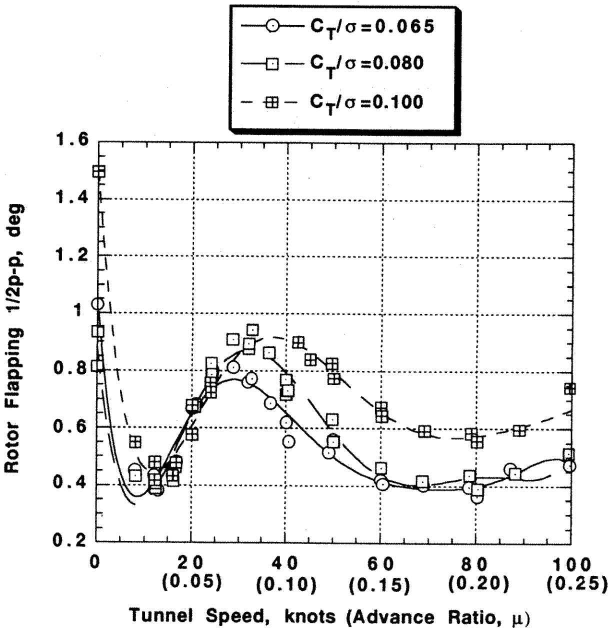

Fig. 24 Effect of advance ratio on rotor 1/2 p-p blade flapping; α_s= -2 deg, C_T/σ=0.065, 0.080, 0.100.